

High-fidelity single-shot readout for a spin qubit via an enhanced latching mechanism

Patrick Harvey-Collard,^{1,2,3,*} Benjamin D'Anjou,⁴ Martin Rudolph,³ N. Tobias Jacobson,⁵
 Jason Dominguez,³ Gregory A. Ten Eyck,³ Joel R. Wendt,³ Tammy Pluym,³ Michael
 P. Lilly,⁶ William A. Coish,^{4,7} Michel Pioro-Ladrière,^{1,2,7} and Malcolm S. Carroll^{3,†}

¹*Département de physique, Université de Sherbrooke, Sherbrooke, QC, J1K 2R1, Canada*

²*Institut quantique, Université de Sherbrooke, Sherbrooke, QC, J1K 2R1, Canada*

³*Sandia National Laboratories, Albuquerque, NM, 87185, United States*

⁴*Department of Physics, McGill University, Montréal, QC, H3A 2T8, Canada*

⁵*Center for Computing Research, Sandia National Laboratories, Albuquerque, NM, 87185, United States*

⁶*Center for Integrated Nanotechnologies, Sandia National Laboratories, Albuquerque, NM, 87185, United States*

⁷*Quantum Information Science Program, Canadian Institute for Advanced Research, Toronto, ON, M5G 1Z8, Canada*

(Dated: February 8th, 2017)

In this work, we study the mechanisms and benefits of an enhanced latching readout for semiconductor spin qubits that generates a signal of larger amplitude, that persists for longer than the conventional spin blockade. The readout of spin states relies on a spin-to-charge conversion mechanism that maps spin states to a transient charge state detected by a charge sensor. We use a silicon quantum dot coupled to a single donor atom to form a singlet-triplet qubit. The asymmetric coupling to charge reservoirs produces latching in the charge transitions. We show that this can be used to extend the lifetime of the charge readout signal by several orders of magnitude. The latched state also produces an enhanced charge signal of one additional electron that improves the signal-to-noise ratio by factors of two, four or even thousands depending on the system's geometry. Using single shot readout, we demonstrate average readout fidelities $> 99.3\%$ and $> 99.86\%$ for the conventional and enhanced readout respectively, the latter being the highest to date for spin blockade. We furthermore highlight that the results apply generally to singlet-triplet and all-exchange qubit systems. This readout relaxes layout constraints because the charge sensor signal is no longer dependent on being aligned with the conventional (2,0)-(1,1) charge dipole.

I. INTRODUCTION

There is a rapidly growing commercial interest in quantum computing for applications such as optimization and quantum chemistry. A number of companies are now attempting to build small quantum bit (qubit) [1, 2] platforms for conceptual testing. Quantum dot spin qubits are of interest because of their promising coherence properties, the solid-state all-electrical control that can be achieved and the potential to be built on the semiconductor fabrication platform already used for high performance computing. Qubit control fidelities have been studied extensively and reached relatively low error probabilities [3–8]. However, state preparation and readout errors have yet to reach similarly low error levels [8–12]. Even though fault tolerance thresholds lie at the 1% level for one error correction round, individual components need to be much better (approximately 0.1% error probability or better). A spin qubit state is measured using a spin-to-charge conversion mechanism that maps spin states to charge states using Pauli spin blockade, followed by readout with a charge sensor (CS) [13]. The minimum achievable error in this readout depends fundamentally on two time scales: the time needed to accurately determine the state and the time for which the excited state can live before relaxing to the ground state. For instance, to achieve a 10^{-3} error

probability, the measurement time should be roughly 10^3 times shorter than the signal lifetime.

In this work, we study an enhanced latching readout mechanism using a silicon quantum dot (QD) coupled to a single donor (D) atom [14]. The two-electron QD-D system can be thought of as a singlet-triplet (ST) qubit [15–17] in an effective double QD configuration [18] where only one of the QDs is connected directly to a charge reservoir [14]. This configuration produces latching (or hysteresis [19]) of the QD-D charge state that can be harnessed to enhance the charge detection [20–22] in two ways. First, the spin states can be mapped to charge configurations that differ by one electron. Compared to the small dipole produced by the traditional readout, this creates a much higher charge signal that is very easily detected by the CS. We show that the CS then doesn't need to be aligned with this charge dipole, which enables detection in configurations where the traditional CS signal would vanish. This has profound implications in terms of design, particularly for QD-D systems and multi-qubit systems where conflicting layout constraints add-up [23]. Second, the latching behavior can extend the lifetime of the charge signal by orders of magnitude by changing the spin relaxation mechanism to a metastable charge relaxation one. Such an improvement can drastically improve detection and could take single-shot readout fidelity well into the fault tolerant threshold regime. The improvement could be particularly pronounced in GaAs where the spin blockade lifetime is $\sim 10 \mu\text{s}$ [24]. We develop a model of the readout mechanisms which is used to ana-

* Correspondance to: P.Collard@USherbrooke.ca

† Correspondance to: mscarro@sandia.gov

lyze the single shot experiments and demonstrate that the enhancement process can lead to an improvement in readout fidelity. We directly compare the benefits of the enhanced latching readout with those of the traditional spin blockade readout by breaking down errors into sequential processes that add together. We leave out errors that could occur during the transit from separated electrons to the spin blockade region (these are studied in other work [9, 18, 24, 25], are common to all readouts and can be made sufficiently small). We account for mapping errors from the additional enhancement processes and from the final CS measurement. We use these techniques to demonstrate a readout fidelity $> 99.86\%$, the highest reported for ST spin blockade so far. Finally, it is worth noting that the results discussed in this work apply not only to donors but to general ST and all-exchange qubit systems where such a charge latching effect can be engineered. These include Si [4, 26, 27], Si/SiGe [17, 28, 29] and GaAs/AlGaAs [16, 30–32].

II. RESULTS

A. Experimental system

The experiments are performed in a silicon metal-oxide-semiconductor (MOS) QD-D device in a dilution refrigerator [14]. A patterned poly-Si gate structure is used to confine electrons at the Si-SiO₂ interface and is shown in Fig. 1(a-b). The device is electrically biased to form a single electron transistor (SET) in the upper wire that is used as a CS, and a few-electron QD in the lower wire. The QD is asymmetrically biased such that it is coupled to a single reservoir. The resulting system is shown schematically in Fig. 1(c). Phosphorus donors have been implanted in a self-aligned way at the location indicated by the red dot. See the “Methods” section for details. Some of the implanted donors are tunnel-coupled to the QD and together with it form an effective double-QD-like system where D states can accommodate a limited number of electrons (e.g. 0, 1).

The absence of direct connection to a charge reservoir for the donor makes it long for the system to relax to the charge ground state via direct tunnelling. As a result, donor electrons can instead go through the QD to exchange with the lead (e.g. Ref. [19] for a double QD version), which can also be relatively slow. This gives rise to a charge latching or hysteresis effect in charge stability diagrams, as shown in Fig. 1(d). Here we denote QD-D charge states by $(N_{\text{QD}}, N_{\text{D}})$, where N_{QD} and N_{D} are the number of electrons on the QD and D, respectively.

The system is tuned around a $(4, 0) - (3, 1)$ QD-D transition which behaves like an effective, spin-blockaded $(2, 0) - (1, 1)$ charge anti-crossing. Details can be found in Ref. [14].

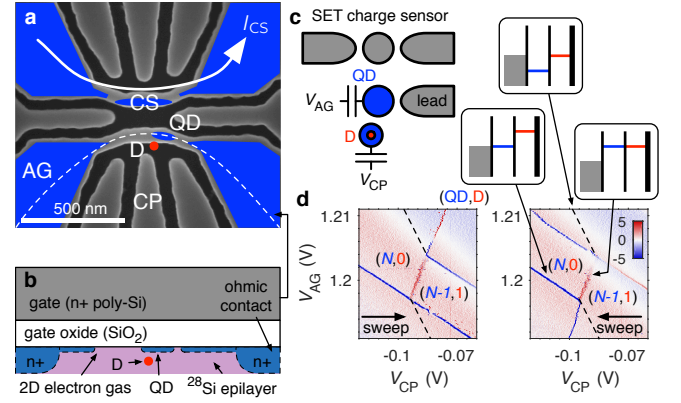


Figure 1. (a) Scanning electron microscope image of the gate structure used to define the QD and CS. The blue overlay indicates the approximate shape of the electron gas. The QD is pushed to the right side and tunnel-coupled to a single reservoir. Phosphorus donors have been implanted in a self-aligned way at the location indicated by the red dot. Some donors are tunnel-coupled to the QD. (b) MOS device gate stack along the dashed line of (a). (c) The QD-D system effectively forms a double-QD-like system where D states have 0 or 1 electrons and have little or no coupling to a charge reservoir. (d) Charge anti-crossing between a QD and a D state. The absence of reservoir for the D makes the charge states latch, which is made apparent by reversing the sweep direction of the scan. The dashed lines indicate where the equilibrium $D \leftrightarrow \text{lead}$ transition should be. Colour scale: $dI_{\text{CS}}/dV_{\text{CP}}$ (a. u.).

B. Readout mechanism

We now show how the naturally-arising latching behavior of QD-D systems can be harnessed to produce a spin readout with very low error rate. To read out a ST qubit, one typically starts with a $(1, 1)$ state, as shown in Fig. 2(a-b). Using fast voltage pulses on the device gates, the electron configuration is brought from point A in $(1, 1)$ to point P in the Pauli spin blockade window [17, 33]. The $(1, 1)S, T_0$ (or $(1, 1) \uparrow\downarrow, \downarrow\uparrow$) states are mapped to either a $(2, 0)S$ or an excited $(1, 1)T_0$ by fast (or slow) adiabatic passage [18]. The CS is used to measure the difference in charge configurations. This process is known as Pauli spin blockade (PSB) spin-to-charge conversion. The net change of charge between the two readout states is zero. For this readout to produce a good signal, the CS needs to be somewhat aligned with the charge dipole. The signal lifetime is determined by the relaxation from the excited $(1, 1)T_0$ to the $(2, 0)S$ ground state. This is typically longer in Si than GaAs systems due to the absence of piezoelectric phonons at the relevant energies, and is a major factor limiting high readout fidelities.

In Fig. 2(a-b), we detail two variations of an enhanced latching readout (ELR), which we call the “direct” and “reverse” variations. The schematics depict a charge anti-crossing with the different charge regions identified. The black thick lines mark fast ground state transitions be-

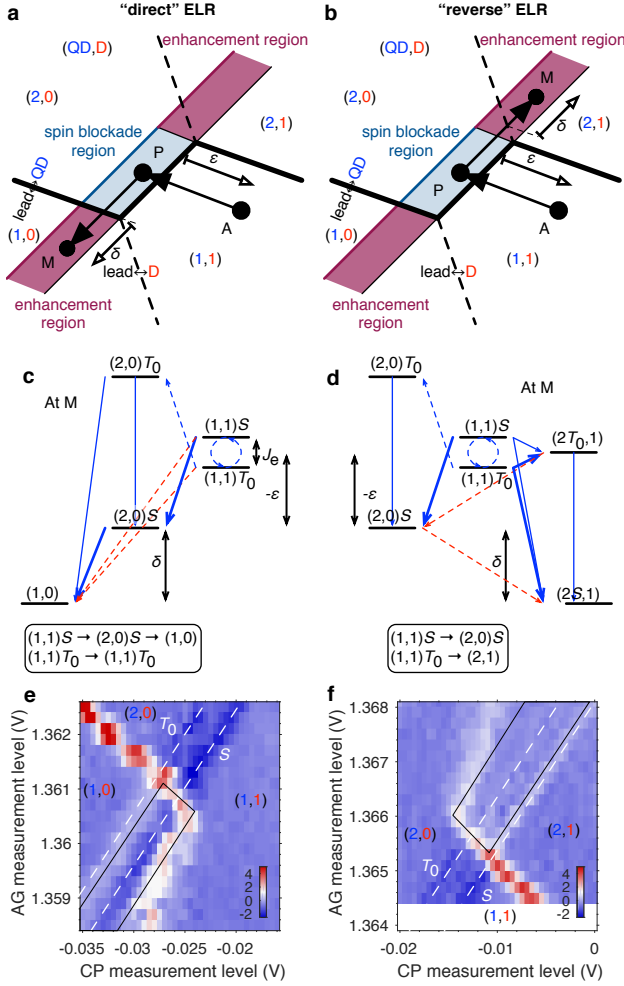


Figure 2. **(a-b)** Two variations of the enhanced latching readout (ELR). In a typical experiment, one would control a ST qubit at point A, and pulse to point P in the Pauli spin blockade (PSB) region for PSB readout (PSBR). From there, an additional pulse to point M for measurement allows the selective mapping of one of the PSB states to a different charge occupation, therefore enhancing the amplitude of the sensed charge signal. Because the $D \leftrightarrow$ lead tunnel rate is very small, the corresponding line in the charge stability diagram can be abstracted out. The thicker black lines represent relatively fast transitions. A nice way to understand the enhancement cause is that the excited state in the PSB region sees a shifted anti-crossing; therefore it does not cross the same $QD \leftrightarrow$ lead transition lines as the ground state for the trajectories considered. **(c-d)** Energy levels and state ladder at point M. The $(1,1)S$ (or $(1,1) \uparrow\downarrow$) is mapped to $(2,0)S$ through fast (or slow) adiabatic passage from A to P. From P to M inelastic tunnelling processes with the lead preform the enhancement. The ϵ and δ parameters can be used to follow the energy detunings throughout the sequence. See main text for details. **(e-f)** A pulse sequence where the M point is swept is used to image the edges of the PSB and enhancement regions. The measurement is averaged and is initialized with a random state. Colour scale: dI_{CS}/dV_{CP} (a. u.).

tween the $QD \leftrightarrow$ lead and the $QD \leftrightarrow D$. The dashed $D \leftrightarrow$ lead line does not play a role due to the charge latching and can be abstracted out in the following reasoning. The PSB region is contained between the $(2,0)S - (1,1)S$ inter-dot degeneracy line (black) and the $(2,0)T_0 - (1,1)T_0$ one (blue). To take advantage of the charge enhancement, one can pulse the gate voltages from point P to one of the regions called “enhancement regions” at point M which are extensions of the PSB region. Because such a pulse crosses one of the fast transition lines, the charge state is rapidly mapped to the corresponding one on the opposite side depending on the state at P. This causes the total number of electrons to differ by one, which generates more signal than the PSB readout (PSBR) and is less geometry-dependent.

1. Direct ELR

We define a direct ELR in which the $(2,0)S$ is mapped to a $(1,0)$ state by inelastic tunnelling with the lead, as shown in Fig. 2(c). The $(1,1)T_0$ is blocked from reaching the $(1,0)$ ground state through $(2,0)$ by the PSB, and cannot rapidly lose the D-side electron to the lead either due to the charge latching. The limiting factor for the signal lifetime is the same as for the PSBR. The signal amplitude corresponds to one additional electron on the donor instead of the $(2,0) - (1,1)$ dipole of the PSBR. We note that the term “direct” is coined because it is possible for the pulse trajectory to go directly from A to M without the detour by P.

We can experimentally reveal the edges of the enhancement and PSB regions (i.e. readout windows) in the Fig. 2(a) by preparing a random state at point A and varying the location of point M in an averaged measurement, as shown in Fig. 2(e). The random state is obtained by loading a $(2,0)S$, fast adiabatic passage through the inter-dot transition, then waiting longer than the coherence time of the qubit. From A with a random state, the voltage is pulsed to point P, then to point M. The location of point M is varied to image the charge regions. The time spent at M is the longest in the pulse sequence, and therefore the signal originates mostly from the charge state at M in this averaging mode.

2. Reverse ELR

In the reverse variation, it is the $(1,1)T_0$ state that is mapped to a $(2,1)$ state by inelastic tunnelling with the lead, as shown in Fig. 2(d). The CS signal is again equivalent to a one electron difference on the donor. This configuration has the significant advantage that the mechanism limiting the lifetime of the signal is transferred to a charge relaxation one that is no longer dependent on the traditionally-limiting PSB relaxation. This can be a significant advantage, particularly in GaAs systems where the PSB lifetime poses significant challenges [24].

We reveal experimentally the edges of the enhancement region using a similar technique as in the direct case. The results are shown in Fig. 2(f).

3. Conditions for enhancement

The state diagrams in Fig. 2(c-d) show important states involved at point M and the transitions between them. The solid lines are used for relatively fast processes, and the dashed lines for relatively slow ones. Blue lines link states involving direct transitions, while red lines represent indirect transitions suppressed by the weak $D \leftrightarrow$ lead tunnel rate (typically Hz). The enhancements in signal and lifetime rely on several conditions to be fulfilled. First, the charge latching must be long-lived so that it does not limit the lifetime of the signal (typically ms). Second, the QD-D inter-dot tunnel coupling t_C (typically GHz) must allow relatively fast transitions so as to allow fast pulses and not introduce a fork or branch in the process ladder. This condition is typically satisfied for working ST qubits due to a fairly large t_C but is important to consider for other types of experimental conditions. Third, the QD \leftrightarrow lead tunnel rate (typically MHz) must be fast enough so as to not be a limiting factor. In the direct ELR variation, a slow $(2, 0) \rightarrow (1, 0)$ event can look like a fast T_0 decay. In the reverse variation, a slow $(1, 1) \rightarrow (2, 1)$ rate can compete with the PSB relaxation rate and introduce a branching process ladder that limits the conversion efficiency.

C. Direct comparison between readouts

We use the anti-crossing featured in Fig. 2 to compare the performance of the readout variations. The data is acquired using the same nominal conditions under a short period of time to allow the best comparison. The donor state involved with this anti-crossing had an inter-dot tunnel coupling large enough to allow adiabatic charge transfer ($\sim 0.5 \mu\text{eV}$), but only with slow detuning ramps ($\sim 10 \mu\text{s}$). These are longer than the qubit coherence time. Nevertheless, it allows us to compare the PSBR and the two ELR variations under the exact same experimental conditions.

We use the average readout fidelity $\bar{F} = 1 - \bar{e}$ as a metric, where $\bar{e} = (e_S + e_T)/2$ is the average error probability for singlets and triplets. Since the scope of this work is to compare the benefits of the ELR with those of the traditional PSB readout, we account for errors that accumulate after the arrival at point P in the PSB window and neglect errors that could occur during the transit from $(1, 1)$ to the PSB region. We account for the additional errors that can occur from P to M as a result of the added complexity and pulses required for the ELR. We call these mapping errors \bar{e}_{map} (these do not apply to the PSB readout). After the pulse arrival at point M, the CS state discrimination process is started, which can also produce

Table I. Comparison of readout parameters between the PSBR and the two ELR variations. The effect of the different relaxation mechanism of the reverse ELR can clearly be seen as it makes the relaxation time over 100 times longer than the PSBR and over 30 times longer than the direct ELR. The main drawback is the branching ratio error contribution to \bar{e}_{map} , which for these specific QD loading and relaxation rates can offset the benefit of the larger and longer signal. Optimizing loading rates could reduce this to a negligible level. While the direct ELR improves the lifetime only moderately (~ 3 times) compared to the reverse ELR, it can still be very useful by reducing the time required for the readout due to the larger signal and typically has a smaller \bar{e}_{map} due to faster unload rates than load ones.

Readout	T_{rel}	\bar{e}_{map}	Signal
PSBR	$300 \pm 80 \mu\text{s}$	0	163 pA
direct ELR	$940 \pm 60 \mu\text{s}$	0.007%	228 pA
reverse ELR	$31 \pm 2 \text{ ms}$	0.07%	220 pA

errors. We call these measurement errors \bar{e}_{meas} . For small errors, the total error \bar{e}_{tot} from composed sequential processes can simply be added, $\bar{e}_{\text{tot}} = \bar{e}_{\text{map}} + \bar{e}_{\text{meas}}$ (see the Supplementary information section “Error composition formula”).

Using single shot readout, we can measure the state relaxation and excitation times T_{rel} and T_{exc} in the different regions [34]. As previously discussed, these times set an upper bound for how fast one should measure to achieve high fidelity. We show the results in Tab. I and Fig. 3. The results clearly show the benefits of the modified reverse ELR relaxation mechanism, which increases T_{rel} by a factor of over 100. The caveat is that the reverse ELR has a branch in the process ladder that results in

$$e_T = \frac{\Gamma_{(2,0)S \leftarrow (1,1)T_0}}{\Gamma_{(2,0)S \leftarrow (1,1)T_0} + \Gamma_{(2,1) \leftarrow (1,1)T_0}}. \quad (1)$$

The effect of the charge enhancement can also be seen in the amplitude of the signal, while the noise remains the same.

According to the schematic of Fig. 2(a), the edges of the readout window should align with those in the PSB region. Experimentally, we find that these are offset a certain amount towards the $(1, 1)$ region in the direct variation (Fig. 2(e)) and towards the $(2, 0)$ region in the reverse variation (Fig. 2(f)). The offset increases as the measurement time is made longer. We also typically observe that the charge latching lifetime during the readout is several orders of magnitude shorter (typically ms) than the $D \leftrightarrow$ lead tunnel rate or cotunnelling processes (typically s). These observations point to the dominant relaxation mechanism being the hybridization of the $(1, 1)$ and $(2, 0)$ states from the tunnel coupling near the inter-dot degeneracy point. As the measurement time is extended, it becomes more likely that the small $(2, 0)$ probability amplitude of the $(1, 1)$ hybridized state allows the system to suddenly jump to the ground state, bypassing the charge

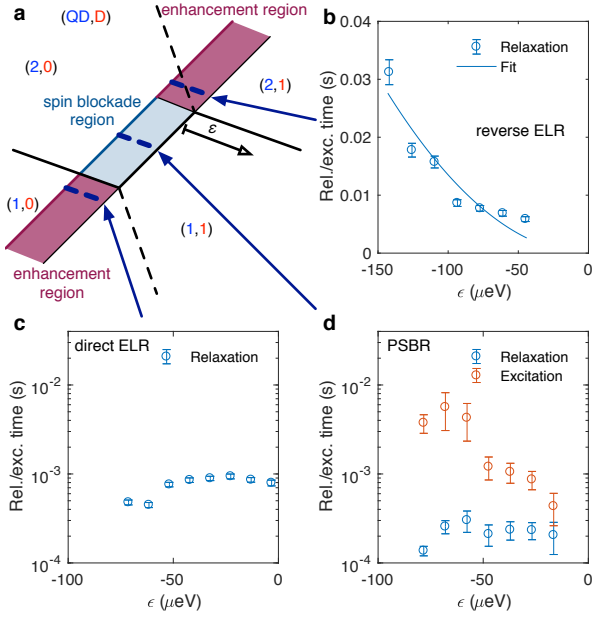


Figure 3. **(a-d)** Relaxation/excitation time versus the detuning ϵ for the different readouts. The data is taken along detuning cuts schematized in (a). The fit in (b) corresponds to a simple relaxation model where the metastable relaxation rate $\Gamma_{\text{MS}} = \Gamma_{(2,1) \leftarrow (1,1)} \beta^2$ and $\beta \approx t_C/\epsilon$ from the inter-dot tunnel coupling t_C (full gap). ϵ is calibrated with the measured lever arm parallel to the QD \leftrightarrow lead transition (32.4 $\mu\text{eV}/\text{mV}$), and the QD loading rate $\Gamma_{(2,1) \leftarrow (1,1)} = 2.56$ MHz is measured independently. The fit yields $t_C = 0.54$ μeV . This value is consistent with independent measurements through diabatic/adiabatic passage experiments.

latching. This effect is observed in the reverse ELR T_{rel} data as well, see Fig. 3(b). We find that it fits a simple relaxation model based on the hybridization between the $(2,0)S$ and $(1,1)S$ states and correctly predicts t_C based on independently measured parameters.

D. High fidelity single shot readout

We now demonstrate that the ELR can achieve higher fidelities than the PSB readout using optimized device parameters and a different donor. The pulse sequence used is shown in Fig. 4(a). As described previously, an averaged measurement technique can be used to image the edges of the readout window, see Fig. 4(c). Using methods described in Ref. [14], we show that this anti-crossing can produce hyperfine-driven coherent rotations between the S and T_0 states, see Fig. 4(b). The visibility of the rotations is low due to experimental bandwidth limits in the pulsing lines (~ 10 ns RC constant), which prevented us from reaching the fast adiabatic passage regime. However, these rotations are presented solely as a justification that the parameter regime chosen for the readout demonstration is appropriate for a ST qubit.

To characterize \bar{F} , we perform an experiment where we

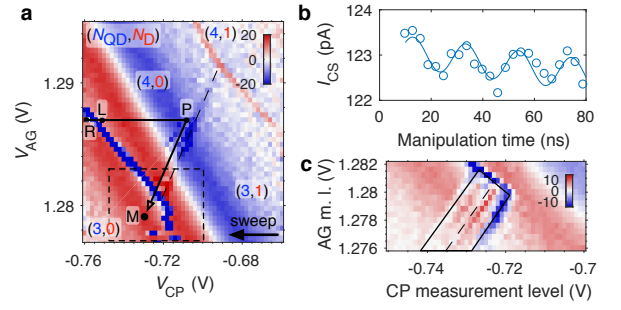


Figure 4. **(a)** Anti-crossing (no pulse applied) and pulse sequence used to demonstrate the high fidelity direct ELR. Colour scale: $dI_{\text{CS}}/dV_{\text{CP}}$ (a. u.). **(b)** This QD-D anti-crossing can produce low-visibility hyperfine-driven coherent rotations as in Ref. [14]. The visibility is limited by the low bandwidth of the pulse compared with the t_C and effective ΔB_z . **(c)** An averaged measurement technique is used to image the edges of the enhancement region by varying the location of the measurement point.

prepare singlets and triplets at random and analyze the process chains for the PSB readout and the direct ELR. Specifically, we first look at errors occurring once the M point is reached. We use this experiment and various others to characterize the parameters of the system (e.g. tunnel rates, relaxation times) and use this information to calculate additional errors \bar{e}_{map} .

We show single shot time traces for the two readouts in Fig. 5(a-b). Those are acquired using the same nominal conditions under a short period of time to allow the best comparison. We define a time t_0 where point M is reached. An approximately 90 μs rise time can be seen in the traces. This is because the readout line has an RC filter that delays the response. As a result, the signal at the beginning of the cycle has memory of the previous one (not shown). This is not ideal and will be addressed in future experiments, although it does not impact our analysis for this particular experiment. We note that we have subtracted a large systematic 820 Hz signal created by the turbo pump on the refrigerator. It is possible to do so because the amplitude and phase are consistent over time, making them predictable in real time using e.g. a Kalman filter [35]. Using post selection, we can determine the average signal for each of the singlet and triplet signals. These are shown as red and blue thick lines. The remaining noise on these traces is well modeled by a Gaussian fit, as shown in Fig. 5(c-d). We observe that the noise is the same for the two readouts, but the signal amplitude is 3.7 times bigger for the ELR case. Using long versions of these traces we can extract the relaxation rates for the excited and metastable states. We then plot the error probability as a function of the time needed to determine the state associated with the signal in Fig. 5(e). The details of the single shot processing are given in the Supplementary information section ‘‘Processing of single-shot charge readout traces’’. The error probability initially goes down as more time allows a more accurate determination.

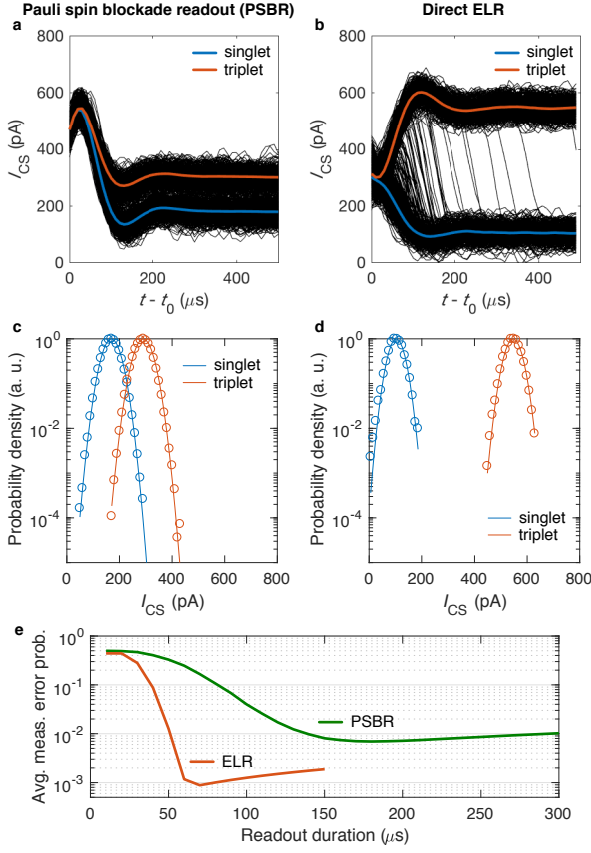


Figure 5. **(a-b)** Single shot time traces for the PSB readout and ELR. The enhancement in signal is clearly visible for the ELR case. **(c-d)** Probability density of finding a certain CS current after the signal is stabilized. It shows the enhancement in signal while the noise magnitude stays the same and is well modeled by a Gaussian fit with standard deviation 268 pA. **(e)** The error probability \bar{e}_{meas} first decreases as the readout duration is increased due to the reduced effect of noise in the state estimation. If the duration is too long, errors from the relaxation/excitation become the dominant source. The ELR shows a factor of 8 enhancement in charge measurement error and 2.3 reduction in measurement time. The limiting factor to the detection time is the limited bandwidth of the system which introduces a significant rise time to the signal.

Moreover, it takes a non-negligible amount of time for the two signals to separate from one another. At longer times, relaxation/excitation events become dominant and limit the error probability. For the PSB readout, we find $T_{\text{rel}} = 15 \pm 3$ ms and $T_{\text{exc}} \sim 300 \pm 200$ ms. The excitation events are rare but not negligible for our low error levels. The excited state population is greater than what is expected from the electronic temperature. This could indicate heating from the pulses or excitations driven by the proximity of the anti-crossing. For the direct ELR, we find $T_{\text{rel}} = 40 \pm 4$ ms and $T_{\text{exc}} \sim 7$ s (from the rare events available). The excitation is found to be negligible for the enhanced case, which is consistent with the larger energy gap that separates the states. The time required for determining the charge is reduced from 150 μ s in the

PSB case to 65 μ s in the ELR case. This 2.3 times improvement is possible because of the larger signal. This in turn reduces the \bar{e}_{meas} from $0.7 \pm 0.1\%$ to $0.088 \pm 0.008\%$, a factor of 8 improvement. This highlights one of the benefits of the ELR.

The various processes contributing to \bar{e}_{map} are detailed in the Supplementary information section “Mapping error for high fidelity result”. We find $\bar{e}_{\text{map}} = 0.048\%$. This comes mostly from a 20 μ s ramp that is used to make sure that the pulse trajectory is carefully followed and is necessary because of the low bandwidth of the AG gate. This could be improved and virtually eliminated with system optimizations. Combining these errors together, we find an average error probability of $\bar{e}_{\text{PSBR}} = 0.7\%$ and $\bar{e}_{\text{ELR}} = 0.136\%$.

As a complementary test, we measure the state preparation and measurement (SPAM) fidelity for pure singlets. Singlet states are prepared by loading the (2,0) ground state, then measured using the procedure previously described. We find a small $e_S < 0.1\%$ over 10^5 cycles. This result is consistent with the stated readout fidelity.

III. DISCUSSION

It is worth noting that the best readout to use depends on the specific details of the system. For instance, in GaAs the PSB relaxation time is typically ~ 10 μ s and fast radio-frequency readouts can measure in ~ 1 μ s [24]. Such a case could clearly benefit from the lifetime enhancement of the reverse ELR. In Si, this relaxation time can be tens of milliseconds. In such a case the better option can be to use the direct ELR, since there is no branching penalty and the signal enhancement allows an improvement in measurement time, as is the case in this work. The amount of signal enhancement depends on the system geometry, and we have observed anywhere from 1.4 times to thousands of times when the inter-dot signal nearly vanishes.

In summary, we have used single shot readout to characterize the fidelity of an enhanced latching readout mechanism. We analyze the cost in fidelity due to the additional charge processes introduced and demonstrate that the enhancement process can actually translate into an improved average readout fidelity. We discuss two variations of the enhancement process that each have benefits and tradeoffs. In the reverse variation, we show that the PSB relaxation mechanism is replaced by a metastable charge relaxation one which can extend the lifetime of the readout signal by a factor of over 100. This could allow significant fidelity improvements particularly in GaAs systems where relaxation is typically fast. We found that the metastable lifetime is limited by the hybridization between the (1,1) and (2,0) states that occurs near the anti-crossing due to the tunnel coupling. Using the direct variation we demonstrate a readout fidelity $> 99.86\%$, the highest reported so far for a spin blockade readout. The enhancement process also allows the CS to be placed

anywhere around the QD, therefore removing a design constraint that could be challenging in donor-based systems or for large arrays of qubits. Basic improvements to the control and readout circuit could take the fidelity well beyond 99.9% in future experiments.

IV. METHODS

A. Device

Electrons are confined in a 2D electron gas at the interface between an epitaxial enriched ^{28}Si layer with 500 ppm residual ^{29}Si and a 35 nm gate oxide. Highly n-doped poly-silicon gates are patterned on top of the gate oxide using low pressure chemical vapor deposition and plasma etching [36]. The gate structure is shown in Fig. 1(a). These are used to accumulate electrons in an enhancement mode by applying a positive voltage or deplete electrons with negative voltages. Phosphorus donors are implanted in a PMMA resist window that overlaps with the AG gate on both sides of both wires, but only the donor location indicated by the red dot in Fig. 1(a-b) is important for this work.

B. Charge sensing and measurements

Experiments are performed in 200 mT (Fig. 2 data) and 300 mT (Fig. 5 data) in-plane magnetic fields. The measured electron temperature is 207 mK. For charge stability diagrams, the current through the CS I_{CS} is measured at 0 V DC bias with a lock-in measurement using an AC excitation of 40 μV RMS (Fig. 2 data) and 100 μV RMS (Fig. 5 data) at 454 Hz. The CS current is then derived numerically to show the sharp steps indicating charge transitions in the QD-D system. The oscillating background in charge stability plots is the Coulomb peaks of the CS. The ST splittings were measured to be 94 μeV (Fig. 2 data) and 222 μeV (Fig. 5 data).

C. Pulsing and single shot

For single shot measurements, the CS is DC-biased with voltages of 100 μV (Fig. 2 data) and 60 μV (Fig. 5 data). For the Fig. 5 data the CS was tuned to have a very narrow and conductive peak to maximize the response. The pulses are applied to the device using a Tektronix AWG7122C arbitrary waveform generator. The pulses are applied through a room-temperature RC bias tee. Waveforms are generated so that all target points are fixed relative to the charge stability diagram except for some parameters that are swept (e.g. measurement point location). The single shot current traces are filtered through an RC cryogenic filter, amplified using a DL 1211 current pre-amplifier, and measured using a Keysight DSO-X 4104A oscilloscope.

ACKNOWLEDGEMENTS

The authors would like to thank Stephen Carr for valuable help regarding this work. P.H.-C. acknowledges funding from Canada's National Science and Engineering Research Council (NSERC). W.A.C. acknowledges funding from NSERC and the Canadian Institute for Advanced Research (CIFAR). This work was performed, in part, at the Center for Integrated Nanotechnologies, an Office of Science User Facility operated for the U.S. Department of Energy (DOE) Office of Science. Sandia National Laboratories is a multi-program laboratory managed and operated by Sandia Corporation, a wholly owned subsidiary of Lockheed Martin Corporation, for the U.S. Department of Energy's National Nuclear Security Administration under contract DE-AC04-94AL85000.

AUTHOR CONTRIBUTIONS

P.H.-C. designed the readout and performed the experiments. B.D. and W.A.C. performed the single shot fidelity analysis. P.H.-C., B.D. and W.A.C. found the dominant metastable relaxation mechanism for the readout. P.H.-C., B.D., W.A.C., M.S.C. and M.P.-L. analyzed and discussed central results throughout the project, including designing experiments and models. M.R. performed supporting measurements on similar control samples that establish repeatability of many observations in this work. N.T.J., P.H.-C. and M.R. modelled key elements of the device structure providing critical insights. J.D., T.P., G.A.T.E. and M.S.C. designed process flow, fabricated devices and designed/characterized the ^{28}Si material growth for this work. J.R.W. performed critical nanolithography steps. M.L. supplied critical laboratory set-up for the work. M.S.C. supervised the combined effort including coordinating fabrication, measurement and modelling. P.H.-C., B.D., M.S.C. and M.P.-L. wrote the manuscript with input from all co-authors.

COMPETING INTERESTS

The authors declare no conflict of interest.

SUPPLEMENTARY INFORMATION

Supplementary information is available.

REFERENCES

- [1] D. Loss and D. P. DiVincenzo, *Phys. Rev. A* **57**, 120 (1998).
- [2] B. E. Kane, N. S. McAlpine, A. S. Dzurak, R. G. Clark, G. J. Milburn, H. B. Sun, and H. Wiseman, *Phys. Rev. B* **61**, 2961 (2000).

- [3] M. Veldhorst, J. C. C. Hwang, C. H. Yang, A. W. Leenstra, B. de Ronde, J. P. Dehollain, J. T. Muhonen, F. E. Hudson, K. M. Itoh, A. Morello, and A. S. Dzurak, *Nat Nano* **9**, 981 (2014).
- [4] M. Veldhorst, C. H. Yang, J. C. C. Hwang, W. Huang, J. P. Dehollain, J. T. Muhonen, S. Simmons, A. Laucht, F. E. Hudson, K. M. Itoh, A. Morello, and A. S. Dzurak, *Nature* **526**, 410 (2015).
- [5] J. T. Muhonen, A. Laucht, S. Simmons, J. P. Dehollain, R. Kalra, F. E. Hudson, S. Freer, K. M. Itoh, D. N. Jamieson, J. C. McCallum, A. S. Dzurak, and A. Morello, *Journal of Physics: Condensed Matter* **27**, 154205 (2015).
- [6] E. Kawakami, T. Jullien, P. Scarlino, D. R. Ward, D. E. Savage, M. G. Lagally, V. V. Dobrovitski, M. Friesen, S. N. Coppersmith, M. A. Eriksson, and L. M. K. Vandersypen, *Proceedings of the National Academy of Sciences* **113**, 11738 (2016).
- [7] K. Takeda, J. Kamioka, T. Otsuka, J. Yoneda, T. Nakajima, M. R. Delbecq, S. Amaha, G. Allison, T. Kodera, S. Oda, and S. Tarucha, *Science Advances* **2**, e1600694 (2016).
- [8] J. M. Nichol, L. A. Orona, S. P. Harvey, S. Fallahi, G. C. Gardner, M. J. Manfra, and A. Yacoby, *npj Quantum Information* **3**, 3 (2017).
- [9] C. Barthel, D. J. Reilly, C. M. Marcus, M. P. Hanson, and A. C. Gossard, *Phys. Rev. Lett.* **103**, 160503 (2009).
- [10] M. D. Shulman, O. E. Dial, S. P. Harvey, H. Bluhm, V. Umansky, and A. Yacoby, *Science* **336**, 202 (2012).
- [11] A. P. Higginbotham, F. Kuemmeth, M. P. Hanson, A. C. Gossard, and C. M. Marcus, *Phys. Rev. Lett.* **112**, 026801 (2014).
- [12] B. Bertrand, H. Flentje, S. Takada, M. Yamamoto, S. Tarucha, A. Ludwig, A. D. Wieck, C. Bäuerle, and T. Meunier, *Phys. Rev. Lett.* **115**, 096801 (2015).
- [13] A. C. Johnson, J. R. Petta, C. M. Marcus, M. P. Hanson, and A. C. Gossard, *Phys. Rev. B* **72**, 165308 (2005).
- [14] P. Harvey-Collard, N. T. Jacobson, M. Rudolph, J. Dominguez, G. A. Ten Eyck, J. R. Wendt, T. Pluym, J. King Gamble, M. P. Lilly, M. Pioro-Ladrière, and M. S. Carroll, *ArXiv e-prints* (2015), arXiv:1512.01606 [cond-mat.mes-hall].
- [15] J. Levy, *Phys. Rev. Lett.* **89**, 147902 (2002).
- [16] J. R. Petta, A. C. Johnson, J. M. Taylor, E. A. Laird, A. Yacoby, M. D. Lukin, C. M. Marcus, M. P. Hanson, and A. C. Gossard, *Science* **309**, 2180 (2005).
- [17] B. M. Maune, M. G. Borselli, B. Huang, T. D. Ladd, P. W. Deelman, K. S. Holabird, A. A. Kiselev, I. Alvarado-Rodriguez, R. S. Ross, A. E. Schmitz, M. Sokolich, C. A. Watson, M. F. Gyure, and A. T. Hunter, *Nature* **481**, 344 (2012).
- [18] J. M. Taylor, J. R. Petta, A. C. Johnson, A. Yacoby, C. M. Marcus, and M. D. Lukin, *Phys. Rev. B* **76**, 035315 (2007).
- [19] C. H. Yang, A. Rossi, N. S. Lai, R. Leon, W. H. Lim, and A. S. Dzurak, *Applied Physics Letters* **105**, 183505 (2014).
- [20] K. D. Petersson, J. R. Petta, H. Lu, and A. C. Gossard, *Phys. Rev. Lett.* **105**, 246804 (2010).
- [21] S. A. Studenikin, J. Thorgrimson, G. C. Aers, A. Kam, P. Zawadzki, Z. R. Wasilewski, A. Bogan, and A. S. Sachrajda, *Applied Physics Letters* **101**, 233101 (2012).
- [22] J. D. Mason, S. A. Studenikin, A. Kam, Z. R. Wasilewski, A. S. Sachrajda, and J. B. Kycia, *Phys. Rev. B* **92**, 125434 (2015).
- [23] T. F. Watson, B. Weber, M. G. House, H. Büch, and M. Y. Simmons, *Phys. Rev. Lett.* **115**, 166806 (2015).
- [24] C. Barthel, J. Medford, H. Bluhm, A. Yacoby, C. M. Marcus, M. P. Hanson, and A. C. Gossard, *Phys. Rev. B* **85**, 035306 (2012).
- [25] P. Cerfontaine, T. Botzem, D. P. DiVincenzo, and H. Bluhm, *Phys. Rev. Lett.* **113**, 150501 (2014).
- [26] J. P. Dehollain, J. T. Muhonen, K. Y. Tan, A. Saraiva, D. N. Jamieson, A. S. Dzurak, and A. Morello, *Phys. Rev. Lett.* **112**, 236801 (2014).
- [27] B. Weber, Y. H. M. Tan, S. Mahapatra, T. F. Watson, H. Ryu, R. Rahman, L. C. L. Hollenberg, G. Klimeck, and M. Y. Simmons, *Nat Nano* **9**, 430 (2014).
- [28] X. Wu, D. R. Ward, J. R. Prance, D. Kim, J. K. Gamble, R. T. Mohr, Z. Shi, D. E. Savage, M. G. Lagally, M. Friesen, S. N. Coppersmith, and M. A. Eriksson, *Proceedings of the National Academy of Sciences* **111**, 11938 (2014).
- [29] K. Eng, T. D. Ladd, A. Smith, M. G. Borselli, A. A. Kiselev, B. H. Fong, K. S. Holabird, T. M. Hazard, B. Huang, P. W. Deelman, I. Milosavljevic, A. E. Schmitz, R. S. Ross, M. F. Gyure, and A. T. Hunter, *Science Advances* **1**, e1500214 (2015).
- [30] S. Foletti, H. Bluhm, D. Mahalu, V. Umansky, and A. Yacoby, *Nat Phys* **5**, 903 (2009).
- [31] L. Gaudreau, G. Granger, A. Kam, G. C. Aers, S. A. Studenikin, P. Zawadzki, M. Pioro-Ladrière, Z. R. Wasilewski, and A. S. Sachrajda, *Nat Phys* **8**, 54 (2012).
- [32] J. Medford, J. Beil, J. M. Taylor, S. D. Bartlett, A. C. Doherty, E. I. Rashba, D. P. DiVincenzo, H. Lu, A. C. Gossard, and C. M. Marcus, *Nat Nano* **8**, 654 (2013).
- [33] A. C. Johnson, J. R. Petta, J. M. Taylor, A. Yacoby, M. D. Lukin, C. M. Marcus, M. P. Hanson, and A. C. Gossard, *Nature* **435**, 925 (2005).
- [34] M. Thalakulam, C. B. Simmons, B. J. Van Bael, B. M. Rosemeyer, D. E. Savage, M. G. Lagally, M. Friesen, S. N. Coppersmith, and M. A. Eriksson, *Phys. Rev. B* **84**, 045307 (2011).
- [35] M. S. Grewal and A. P. Andrews, *Kalman Filtering: Theory and Practice Using MATLAB*®, 2nd ed. (John Wiley & Sons, Inc., 2002).
- [36] L. A. Tracy, T. M. Lu, N. C. Bishop, G. A. Ten Eyck, T. Pluym, J. R. Wendt, M. P. Lilly, and M. S. Carroll, *Applied Physics Letters* **103**, 143115 (2013).

V. SUPPLEMENTARY INFORMATION

A. Error composition formula

In this section, we derive formulas for the composition of classical and independent error processes in series. We assume two classical states S and T . Let e_S and e_T be the probability that S flips to T , and T flips to S , respectively. We define an average error probability $\bar{e} = (e_S + e_T)/2$. Let $\bar{e}' = (e'_S + e'_T)/2$ be the error probabilities for a second process occurring in series after the first process. The total error of these two processes in series is such that $e''_S = v'e_S + e'_S$, $e''_T = v'e_T + e'_T$, with $v' = 1 - e'_S - e'_T$. The total average error probability is then $\bar{e}'' = \bar{e}' + \bar{e} - 2\bar{e}'\bar{e}$. If $\bar{e}', \bar{e} \ll 1$, the second order term can be neglected and the average errors simply add, $\bar{e}'' \approx \bar{e}' + \bar{e}$.

B. Mapping error for high fidelity result

Errors can occur from the diabatic crossing of the $(2,0) - (1,1)$ charge transition. The visibility of the ST rotations allows to estimate the inter-dot t_C to be $\gtrsim 20 \mu\text{eV}$ (full gap at degeneracy point). This is sufficiently high to avoid any issues related to diabatic crossing with respect to charge.

Next, we look at the unload rate of the $(2,0)S$ state, $\Gamma_{(1,0) \leftarrow (2,0)S}$. Using a detailed model for excited state spectroscopy, we extract a lower bound for this rate and find $1/\Gamma_{(1,0) \leftarrow (2,0)S} < 2.5 \mu\text{s}$. We estimate that for $t - t_0 = 13 \mu\text{s}$, and knowing that when t_0 is reached the system has already spent $10 \mu\text{s}$ in the $(1,0)$ region due to the ramp, the probability for a singlet to be read out as a decaying triplet is $< 1 \times 10^{-4}$. This adds a rather small delay to the charge signal in a $< 1 \times 10^{-4}$ number of cases (for singlets only) compared to other error sources. It is therefore not a significant error source.

The possible decay of triplets before t_0 can also be a source of errors. Those decaying after are accounted for in the measurement error \bar{e}_{meas} . For this experiment we use a fairly long $20 \mu\text{s}$ ramp to go from P to M. This is done to make sure that the pulse trajectory is carefully followed and is necessary because of the low bandwidth of the AG gate. This could be improved and virtually eliminated with system optimizations. The system spends $10 \mu\text{s}$ in the PSB region before crossing over to the enhancement region. This allows for some triplets to relax to singlets and some singlets to be excited to triplets before the enhancement. Considering the relaxation/excitation rates found in the PSB readout, this process adds a $e_T = 0.67 \times 10^{-3}$ and $e_S = 0.033 \times 10^{-3}$ error probability before the enhancement region. In the enhancement region, the triplet decay probability is estimated using the decay rate in the enhanced region, and is $e_T = 0.25 \times 10^{-3}$. The singlet excitation before $(2,0)S$ it is mapped to $(1,0)$ is given by a branching ratio between $\Gamma_{(1,0) \leftarrow (2,0)S}$ and $\Gamma_{(1,1)T_0 \leftarrow (2,0)S}$ and is $e_S = 0.01 \times 10^{-3}$.

Finally, we look at thermal excitation of $(1,1)T_0$ into $(2,0)T_0$ followed by an immediate decay into $(1,0)$. We suspect from the long lifetime measured that this is not an issue. We nevertheless estimate through detailed balance that the excitation rate is $0.1 \times 10^{-3} \times \Gamma_{(1,1)T_0 \leftarrow (2,0)T_0}$. Though we do not measure this rate, if we assume it is governed by a similar mechanism as PSB relaxation, it should be several seconds and therefore negligible.

The total average mapping error is therefore 0.048%.

C. Processing of single-shot charge readout traces

1. Removing unwanted signal from turbo pump

The acquired single-shot readout traces were distorted by a periodic signal of frequency $\sim 820 \text{ Hz}$ generated by a turbo pump. This signal complicates the interpretation of the readout statistics. While it would be ideal to directly isolate the readout chain from this spurious signal, here we show that we can demonstrate single-shot readout capability even when it is present.

Since the signal is periodic, we can expand it in a Fourier series:

$$s_{\text{TP}}(t) = \sum_{k=1}^{\infty} A_k \cos[2\pi k f t + \phi_k] \quad (2)$$

where $f \approx 820 \text{ Hz}$ is the pump signal frequency and where A_k and ϕ_k are the amplitudes and phases of the pump signal harmonics. We wish to estimate the parameters f , $\{A_k\}$, and $\{\phi_k\}$.

Since the pump signal period is smaller than but comparable to the duty cycle of the single-shot readout, we need to estimate the parameters in Eq. (2) over many such cycles while tracking the phase of the oscillations. Fig. 6a shows a subset of ~ 18 single-shot readout cycles for the Pauli spin blockade readout of Sec. II D. To isolate the effect of the pump signal from the readout signal, we postselect time intervals within each cycle where the charge state has relaxed and where the initial transient response of the charge sensor (seen in Figs. 7a-b) has disappeared.¹ These time intervals are shown in Fig. 6a. We then subtract the average charge signal of the selected time intervals to obtain a pump signal of the form in Eq. (2), as illustrated in Fig. 6b. We perform a similar analysis for the enhanced latching readout.

To maintain real-time single-shot readout capability, it is desirable to have the ability to remove the pump signal

¹ More precisely, we first select cycles for which the time-averaged current over a pump period and the maximum charge sensor current on the period are both below a threshold (chosen intermediate between the two charge sensor readout signals). For each of these cycles, we keep a short time interval at the end of the cycle where the initial transient response of the charge sensor has disappeared.

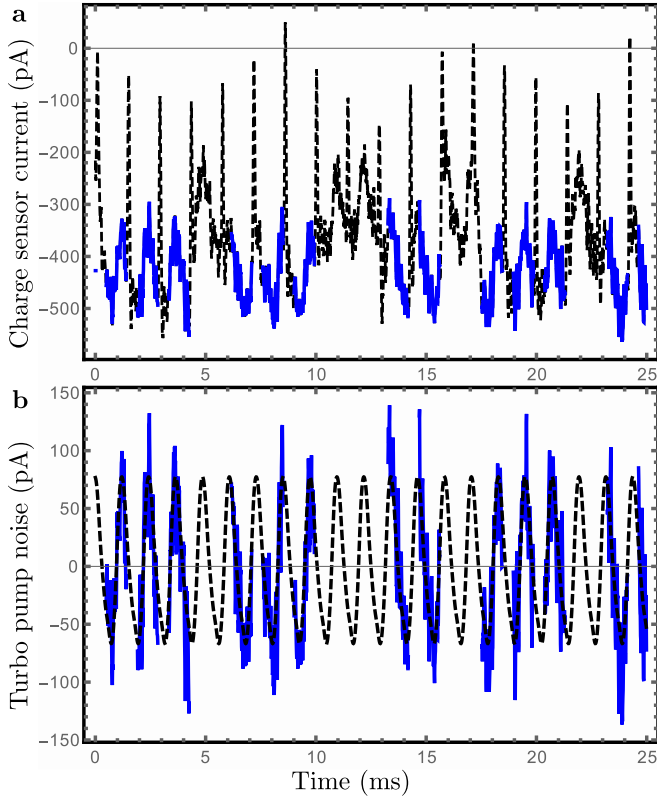


Figure 6. **(a)** A few (~ 18) single-shot readout cycles (dashed black line). For each cycle, we extract a time interval where the charge state has relaxed and where the initial transient response of the charge sensor has disappeared (solid blue line). **(b)** Resulting measured turbo pump signal (solid blue line) and fit obtained using the Kalman filter (dashed black line).

in real time. We show that this is possible by fitting the extracted pump signal to Eq. (2) over a large number of cycles (typically $\gtrsim 10^3$) using an extended Kalman filter. The extended Kalman filter performs a least squares fit to Eq. (2) in real-time, demonstrating the ability to estimate and remove the turbo pump signal on-the-fly. The fit accurately reproduces the measured signal, as can be seen in Fig. 6b. We find that it is sufficient to keep the first 5 terms in Eq. (2). We also find that the pump signal parameters do not drift substantially over the acquisition period.

Finally, we subtract the fitted signal from the entire readout sequence. The resulting single-shot readout traces are those shown in, e.g., Fig. 5(a-b).

2. Estimating the charge sensor signal and noise

Estimating the charge readout fidelity requires a precise understanding of the charge sensor signal and noise conditioned on the initial charge state. To characterize the signal and noise for each state, we postselect the single-shot readout cycles for which no relaxation or excitation

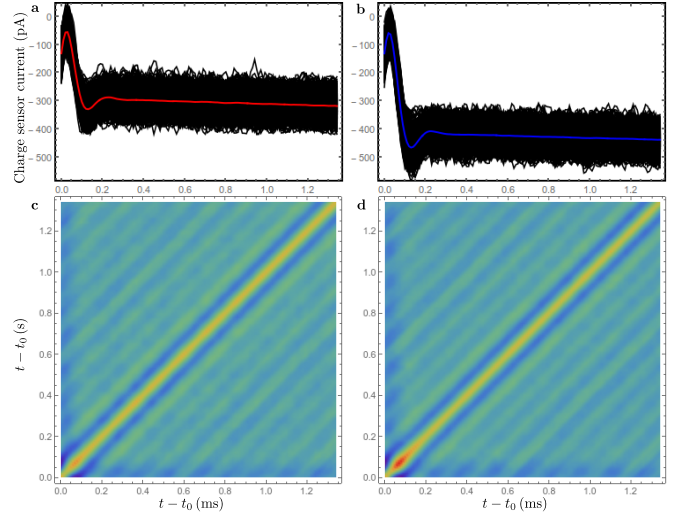


Figure 7. **(a-b)** Single-shot traces postselected on the absence of relaxation or excitation (solid black) for the Pauli spin blockade readout of Sec. IID. We also show the mean signal for the (1,1) charge state (solid red) and the (2,0) charge state (solid blue). The persistent slant in the sensor response is attributed to a bias-tee transient, as discussed in Sec. VC3. **(c-d)** Covariance matrices of the noise postselected on the (1,1) charge state, (c), and on the (2,0) charge state, (d). Time is measured from t_0 , the time of arrival at the measurement point.

occurs.² The two sets of postselected traces are illustrated in Fig. 6a-b for the Pauli spin blockade readout of Sec. IID. We perform the same analysis for the enhanced latching readout.

From the postselected traces, we can immediately extract the mean sensor signal, as shown in Fig. 7a-b. We then verify that the noise has Gaussian statistics by making a histogram of the fluctuations of the charge sensor current around the mean (see Fig. 5(c-d) in the main text). Gaussian noise is completely characterized by its covariance. We thus calculate the covariance matrix of the noise for the two possible charge states. As illustrated in Fig. 7c-d, the covariance matrices capture non-stationary features of the noise (greater noise during the finite signal rise time) and non-Markovian features of the noise (oscillations along the off-diagonal of the covariance matrix). We account for all these features in our charge readout fidelity estimate (see Sec. VC4).

3. Estimating the relaxation time

The charge readout fidelity is ultimately limited by the finite integration time set by the relaxation and ex-

² We select readout cycles for which the maximum (minimum) charge sensor current over the time interval where the two charge signals can be discriminated is below (above) a threshold (chosen to be intermediate between the two charge sensor readout signals).

citation processes. Suppose the charge sensor signals for both possible initial charge states, say $|+\rangle$ and $|-\rangle$, are constants I_+ and I_- . We can then extract the relaxation rate $\Gamma_{\text{rel.}}$ from $|+\rangle$ to $|-\rangle$ and the excitation rate $\Gamma_{\text{exc.}}$ from $|-\rangle$ to $|+\rangle$ by fitting the ensemble average of the single-shot readout traces, $\langle I_{\text{CS}}(t) \rangle$, to an asymmetric telegraph process:

$$\begin{aligned} \langle I_{\text{CS}}(t) \rangle &= Ae^{-\Gamma t} + B, \\ \Gamma &= \Gamma_{\text{rel.}} + \Gamma_{\text{exc.}}, \\ B &= \frac{\Gamma_{\text{exc.}}}{\Gamma} I_+ + \frac{\Gamma_{\text{rel.}}}{\Gamma} I_-. \end{aligned} \quad (3)$$

Note that Eq. (3) assumes that the charge dynamics involves only two states. Depending on the system parameters (such as detuning, tunnel coupling, or donor hyperfine coupling), this may not always be a good approximation. Nevertheless, we verified that our fitting procedure gives results consistent with direct counting of the number of relaxation and excitation events.

Fig. 8a shows the measured charge sensor signals in the absence of relaxation or excitation for both charge states (see Sec. VC2) for the Pauli spin blockade readout of Sec. IID (where $|+\rangle = (1, 1)$ and $|-\rangle = (2, 0)$). The measurement conditions are the same as in Fig. 7a-b, but with a single-shot duty-cycle of 30 ms instead of 1.4 ms. The charge sensor signal changes over time, which we attribute to (possibly charge-state dependent) bias-tee transients (see Sec. IVC). Both transients are fit to an exponential and I_{\pm} are extracted from the long-time behavior³. To fit the average single-shot signal to Eq. (3), we first rescale $\langle I_{\text{CS}}(t) \rangle$ to remove the effect of the transients. The corrected average is shown in Fig. 8b along with the fit to Eq. (3). We perform a similar procedure for the enhanced latching readout.

For the Pauli spin blockade readout, charge excitation is observed in a non-negligible fraction of readout cycles. For the enhanced latching readout, however, there are almost no instances of excitation. Therefore, we leave B as a free fit parameter for the Pauli spin blockade readout and we set $B = I_-$ for the enhanced latching readout. We speculate that the excitation in the Pauli spin blockade readout is generated by environmental electric field fluctuations of unknown origin coupling to the $(2, 0) \rightarrow (1, 1)$ dipole transition. This excitation mechanism is suppressed in the enhanced latching readout because an electron must first be exchanged with the low-temperature reservoir before such a dipole transition can occur. Charge excitation in the direct enhanced latching readout, for example, first requires the transition from $(1, 0)$ to $(2, 0)$, followed by a transition from $(2, 0)$ to $(1, 1)$ before the charge state has a chance to go back to $(1, 0)$.

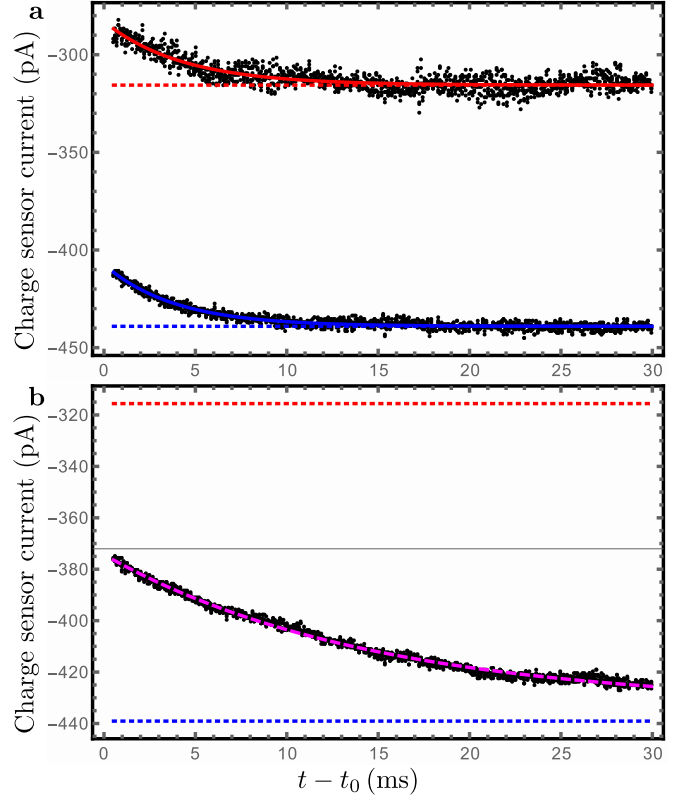


Figure 8. (a) Observed time dependence of the charge sensor signal for both initial charge states (black dots) for the Pauli spin blockade readout of Sec. IID. We fit the signals to extract the transients for $|+\rangle = (1, 1)$ (solid red) and for $|-\rangle = (2, 0)$ (solid blue). The long-time behavior of the fit gives I_+ (dotted red) and I_- (dotted blue). (b) Average of the single-shot traces (black dots) after correction for the transients. In general, the average decays to some value between I_+ (dotted red) and I_- (dotted blue).

The precision on our estimates of $\Gamma_{\text{rel.}}$ and $\Gamma_{\text{exc.}}$ is limited by the statistical fluctuations in $\langle I_{\text{CS}}(t) \rangle$ due to the finite number of single-shot traces. We thus estimate the error bars on the fit parameters Γ , A , and B by calculating the Fisher information matrix of the parameters with respect to the assumed telegraph process. Note that since the noise in the telegraph process is correlated on a time scale Γ^{-1} , the parameter we want to estimate, it is important to account for temporal correlations of the telegraph process in the estimate of the error bar. Not accounting for these correlations underestimates the error bar by an order of magnitude.

4. Charge readout fidelity bound

Knowing the signal, noise, and relaxation and excitation rates, we can obtain an upper bound on $\bar{e}_{\text{meas.}}$. In the following, we count errors from t_0 , the time of arrival at the measurement point. Additional mapping errors are discussed in Sec. VB.

³ In cases where there is not enough data available (i.e. too much statistical noise) to accurately fit to an exponential behavior, the transients are fit to a constant instead.

If the charge state is initially $|+\rangle$, the error probability is bounded by:

$$\begin{aligned}
e_{\text{meas.},+} &= P(\text{err.}|+, \text{rel.})P(\text{rel.}|+) \\
&\quad + P(\text{err.}|+, \text{no rel.})P(\text{no rel.}|+), \\
e_{\text{meas.},+} &< P(\text{rel.}|+) + P(\text{err.}|+, \text{no rel.})P(\text{no rel.}|T), \\
e_{\text{meas.},+} &< 1 - e^{-\Gamma_{\text{rel.}}(t-t_0)} \\
&\quad + P(\text{err.}|+, \text{no rel.})e^{-\Gamma_{\text{rel.}}(t-t_0)} \\
&= e_{\text{meas.},+}^B.
\end{aligned} \tag{4}$$

Similarly, when the charge state is initially $|-\rangle$, the error probability is bounded by:

$$\begin{aligned}
e_{\text{meas.},-} &< 1 - e^{-\Gamma_{\text{exc.}}(t-t_0)} \\
&\quad + P(\text{err.}|-, \text{no exc.})e^{-\Gamma_{\text{exc.}}(t-t_0)} \\
&= e_{\text{meas.},-}^B.
\end{aligned} \tag{5}$$

The average error probability is bounded by:

$$\begin{aligned}
\bar{e}_{\text{meas.}} &= \frac{1}{2}(e_{\text{meas.},+} + e_{\text{meas.},-}) \\
&< \frac{1}{2}(e_{\text{meas.},+}^B + e_{\text{meas.},-}^B).
\end{aligned} \tag{6}$$

Eqs. (4), (5), and (6) give a bound on the average error probability in the presence of relaxation and excitation, given the error probabilities in the absence of relaxation or excitation, $P(\text{err.}|+, \text{no rel.})$ and $P(\text{err.}|-, \text{no exc.})$. In the following, we obtain Monte-Carlo estimates of $P(\text{err.}|+, \text{no rel.})$ and $P(\text{err.}|-, \text{no exc.})$.

Let $n = (t - t_0)/\delta t$ be the number of measurement time bins, where δt is the sampling time. In the absence of relaxation (excitation), the vector signal I_n for the $|+\rangle$ ($|-\rangle$) charge state is a multivariate Gaussian random variable with mean signal μ_+ (μ_-) and covariance matrix C_+ (C_-). These quantities are directly measured as described in Sec. VC2. Formally, we have:

$$\begin{aligned}
P(I_n|+, \text{no rel.}) &= \frac{1}{\sqrt{(2\pi)^n |C_+|}} e^{-\frac{1}{2}(I_n - \mu_+)^T C_+^{-1} (I_n - \mu_+)}, \\
P(I_n|-, \text{no exc.}) &= \frac{1}{\sqrt{(2\pi)^n |C_-|}} e^{-\frac{1}{2}(I_n - \mu_-)^T C_-^{-1} (I_n - \mu_-)}.
\end{aligned} \tag{7}$$

We simulate the readout in the absence of relaxation and excitation in the following way. For each readout time and for both initial states, 10^6 random signals I_n are randomly sampled from the distributions of Eq. (7). Eq. (7) is then used to decide which state most likely produced the random signal. Counting the number of errors for each charge state gives $P(\text{err.}|+, \text{no rel.})$ and $P(\text{err.}|-, \text{no exc.})$. An upper bound on the error rate is then obtained using Eqs. (4), (5), and (6). These are the bounds illustrated in Fig. 5(e).